Research Article Vol. 10, No. 4 / April 2023 / Optica 443

Dynamic freeform diffractive lens

Omel Mendoza-Yero

Institut de Noves Tecnologies de la Imatge (INIT), Universitat Jaume I, 12080 Castelló, Spain (omendoza@uji.es)

Received 19 December 2022; revised 24 February 2023; accepted 3 March 2023; published 31 March 2023

In the framework of the scalar theory of diffraction a surface-pixeled convergent lens for arbitrary amplitude and phase modulation along the depth of focus is introduced. This complex diffractive lens is computer-generated from an exact solution of the inverse focal shaping problem obtained by using the Fresnel diffraction integral. The spatial multiplexing technique of the double-phase method is employed to encode the complex diffractive lens into a phase optical element that can be dynamically implemented with a commercial liquid-crystal spatial light modulator. The optical surface of this lens, capable of generating not only a single axial focus but also multiple parallel foci, has neither linear nor rotational symmetry but phase jumps from one pixel to another. In addition to intensity shaping, the introduced lens provides simultaneous control over the phase of light along the depth of focus, which can be very attractive for improving and/or developing photonic applications related to the interaction of coherent laser beams with matter.

https://doi.org/10.1364/OPTICA.484048

1. INTRODUCTION

Beam shaping is a prerequisite for most photonics applications [1–5]. Starting from an input laser beam with known optical features, the shaping should be able to generate an output laser illumination with prescribed characteristics. Hence, beam shaping can be through a solution of an inverse problem (IP) that determines the proper optical surfaces to get desired illumination [2,6]. For many laser applications, having user-defined intensity distributions may be sufficient to achieve the expected results. For this reason, beam shaping is often associated only with amplitude modulation [7–9]. However, because laser beams are described by complex mathematical expressions, full control over them can only be achieved if we are able to change their intensity and wavefront (phase) at will, simultaneously. This shaping procedure is known as complex beam shaping (CBS) [10–14].

Recently, freeform optics has become a technology in high demand for CBS [15–17]. Nonetheless, for intensity and wavefront modulation, at least two optical surfaces without linear or rotational symmetry must be designed, measured, and fabricated [18–20]. The design of these freeform surfaces remains an open problem faced by researchers today by using different methods, such as the calculus of a nonlinear partial differential equation [21], the use of the geometric supporting quadric method [22], or the ray mapping method based on an optimal mass transportation problem with a quadric cost function [23]. In practice, reflective and refractive optical elements fabricated by freeform optics are relatively easy to implement and can achieve high energy transfer efficiency, but their optical end surfaces cannot be changed dynamically. In addition, it is well-known [24–27] that bulk optics is unable to efficiently manipulate laser radiation at certain frequencies forbidden by scattering or light absorption. For instance, when dealing with ultrashort lasers, the unwanted optical breakdown phenomenon may induce damage in materials due to nonlinear absorption of energy [26,27]. In this context, diffractive optics can be regarded as a user-friendly alternative to perform CBS. Specifically, diffractive optical elements (DOEs) have demonstrated high-performance and suitable characteristics for beam shaping purposes [28–30], i.e., small thickness, low weight, high efficiency, and high accuracy in manufacturing. On the other hand, the latest generation of spatial light modulators (SLMs) [31–33] allows dynamic beam shaping at frequencies up to MHz.

Under the frame of the scalar theory of diffraction, the on-axis electric field associated with focused laser beams can be engineered by means of diffractive amplitude and phase pupils acting as optical filters [34]. For circularly symmetric pupils, this electric field can be related to the one-dimensional Fourier transform (FT) of a complex pupil function expressed in the squared radial coordinate [35]. The calculus of a single FT operation significantly decreases computation times, while establishing a unique solution for the IP, which is directly related to the computer generation of such complex functions. Furthermore, the use of phase-only (pho-SLMs) guaranties the dynamic implementation of complex pupils with enhanced light efficiencies in comparison with other types of SLMs, i.e., a digital micromirror device. Nevertheless, for working with phase-only optical devices the complex pupils must be properly encoded into phase masks. One method proposed to do that employs two spatial light modulators (SLMs) to separately display the amplitude and phase information of complex pupils [36]. In another method, the diffraction efficiency of phase filters has been properly changed to accomplish amplitude modulation [37]. It allows the amplitude of complex pupils to be encoded into twisted nematic liquid-crystal SLMs to synthesize on-axis intensity patterns [38]. Recently, by taking advantage of the double-phase

method (DPM) [39–43], an exact solution for axial IP was found [44]. This solution can be considered as an extension of the so-called theory of complex pupils, providing not only intensity but also wavefront modulation, simultaneously. However, from a practical point of view, the need for a spatially filtered 4f optical system to reconstruct the complex pupil or the alignment requirements with respect to the focusing element may limit the use of the focal CBS method.

In this paper, a freeform diffractive lens (FFDL) for arbitrary CBS of coherent laser beams along the depth of focus is introduced. In contrast with a conventional diffractive lens, i.e., Fresnel lens that tailors the intensity of the laser beams only, the introduced FFDL can axially modulate both the amplitude and phase of the on-axis electric field at the focal region, simultaneously. The proposed beam shaping method implies several benefits that include fast, complete, and deterministic beam shaping algorithm based on an exact solution of the IP, reduced thickness and optical setup dimensions, high accurate, efficiency and versatile operation, and direct practical realization with programmable pho-SLM. The physical behavior of the FFDL was corroborated with experiments aimed to measure the prescribed on-axis intensity profile and axial phase of a quasi-monochromatic laser beam focused by different FFDLs. In all cases, numerical simulations and experiments agree well, achieving values of root-mean-square-errors (RMSE) below 10%.

2. MATHEMATICAL MODEL

In this section, the mathematical formulation and design procedure of the FFDL are presented. The on-axis electric field $E(z)$ along the focus of a convergent lens of focal length f and radius a, can be described by the Fresnel diffraction integral written in Cartesian coordinates:

$$E(z) = \frac{2\pi}{iz\lambda}\iint_{-a}^{a} q(\xi,\eta)\, e^{\frac{i\pi}{\lambda z}(\xi^2+\eta^2)}\,\mathrm{d}\xi\,\mathrm{d}\eta, \tag{1}$$

where the focusing element $q(\xi,\eta)$ is defined as

$$q(\xi,\eta) = p(\xi,\eta)\, e^{-\frac{i\pi}{\lambda f}(\xi^2+\eta^2)}. \tag{2}$$

In Eq. (1), the plane wave term $e^{i\frac{2\pi}{\lambda}z}$ was not considered. The axial coordinate is given by z, and λ is the wavelength of light in vacuum. The quadratic exponential term $\pi(\xi^2+\eta^2)/(\lambda f)$ in Eq. (2) denotes the phase of the convergent lens with complex pupil $p(\xi,\eta)$ under the thin lens approximation. By using Eqs. (1) and (2), one can modify the axial electric field $E(z)$ associated with the focused laser beam by engineering the focusing element $q(\xi,\eta)$. However, to do that in a prescribed manner it is necessary to invert Eq. (1), expressing the focusing element $q(\xi,\eta)$ as a function of the electric field $E(z)$. After doing some mathematical manipulations to Eq. (1), it can be shown that the solution of the IP yields [44]:

$$q(s) = \frac{i}{2\pi}\mathcal{F}^{-1}\left\{\frac{E(u)\, e^{-i\pi(u-u_0)}}{u}\right\}. \tag{3}$$

To obtain Eq. (3), no assumptions or approximations have been done. The symbol $\mathcal{F}^{-1}$ denotes the inverse FT operation, whereas the normalized variable $u = a^2/(2\lambda z)$, and the constant $u_0 = a^2/(2\lambda f)$. The focusing element $q(s)$, expressed in the squared radial coordinate $s = r^2/a^2 - 1/2$ with $s \in [-1/2,\ 1/2]$, can cause on-axis electric field focalization with user-defined amplitude $A(u)$ and phase $\Theta(u)$ features. To clearly identify these terms in Eq. (3), the electric field is rewritten in the form $E(u) = A(u)e^{i[\pi(u-u_0)+\Theta(u)]}$, consequently the solution of the IP is reduced to the expression

$$q(s) = \frac{i}{2\pi}\mathcal{F}^{-1}\left\{\frac{A(u)\, e^{i\Theta(u)}}{u}\right\}. \tag{4}$$

Once the focusing element $q(s)$ is calculated from Eq. (4), the transformation of this vector $q(s) \to q(r)$ from squared to radial coordinate is carried out. In addition, the rotation of $q(s)$ and $q(r)$ around their origins permits to digitally construct corresponding two-dimensional amplitude and phase masks. The complex focusing element $q(x,y)$, expressed for convenience in the Cartesian coordinates x, y, cannot be directly sent to the pho-SLM. To overcome this limitation, the spatial multiplexing technique of DPM is used to encode $q(x,y)$ into a single-phase element. So, it is rewritten in terms of two uniform waves $e^{i\theta(x,y)}$ and $e^{i\vartheta(x,y)}$ as follows:

$$q(x,y) = \Lambda(x,y)\, e^{i\phi(x,y)} = e^{i\theta(x,y)} + e^{i\vartheta(x,y)}, \tag{5}$$

where

$$\theta(x,y) = \phi(x,y) + \cos^{-1}[\Lambda(x,y)/\Lambda_{\max}], \tag{6}$$

$$\vartheta(x,y) = \phi(x,y) - \cos^{-1}[\Lambda(x,y)/\Lambda_{\max}]. \tag{7}$$

To obtain Eq. (5), the constant term $\Lambda_{\max}$ given in Eqs. (6) and (7) was set to 2. This constant term is the maximum value of the amplitude function $\Lambda(x,y)$, whereas the phase associated to the focusing element is denoted by $\phi(x,y)$. Then, the above uniform waves are spatially mapped with two complementary binary gratings $M_1(x,y)$ and $M_2(x,y)$, taken at the Nyquist limit, such as $M_1(x,y) + M_2(x,y) = 1$, in the following manner:

$$M_1(x,y)\, e^{i\theta(x,y)} + M_2(x,y)\, e^{i\vartheta(x,y)} = e^{i\alpha(x,y)}, \tag{8}$$

where

$$\alpha(x,y) = M_1(x,y)\,\theta(x,y) + M_2(x,y)\,\vartheta(x,y). \tag{9}$$

At this point, one might realize that the uniform wave $e^{i\alpha(x,y)}$ given in Eq. (8) can be used to emulate the diffraction effects of the focusing element $q(x,y)$ in Eq. (1). This can be better understood if we assume that the impact of $e^{i\alpha(x,y)}$ on the electric field $E(z)$ does not depend on the sampling order originated by the interchange of binary gratings $M_1(x,y)$ and $M_2(x,y)$ in Eq. (9). This assumption holds when the sampling frequency is high enough to ensure full recovery of the sampled functions after a simple interpolation operation. Under the above assumption, it can be easily shown that $E(z) = 2E_\alpha(z)$, where the electric field $E_\alpha(z)$ is determined by Eq. (1) after substituting the focusing element $q(x,y)$ by the uniform wave $e^{i\alpha(x,y)}$. However, when performing CBS with the phase grating $\alpha(x,y)$ the diffracted light is redistributed among the different diffraction orders of this grating, being the zero order the focus of the introduced lens. Consequently, the available energy at the focus decreases with respect to the ideal situation that comes from the coherent interference of the uniform waves $e^{i\theta(x,y)}$ and $e^{i\vartheta(x,y)}$. The phase-only element $\alpha(x,y)$ defined by Eq. (9) is called FFDL. The experimental implementation of FFDL is free from additional optical setups, i.e., 4f imaging

optical system. In addition, the integration of the complex pupil $p(x, y)$ within the focusing lens provides a really compact and versatile DOE. These advantages will be experimentally corroborated in the next section. In Fig. 1, the whole process involving the design of the FFDL is illustrated with an example. It begins with the selection of the desired amplitude and phase of the complex field along the depth of focus. In this example, they are given by the triangular function $A(u) = 1 - |u|$, and the cubic phase $\Theta(u) = \pi u^3$. The number of sampling points N is determined from the difference $N = a^2/[2\lambda(f - \Delta z/2)] - a^2/[2\lambda(f + \Delta z/2)]$, where Δz is the focal depth. After using Eq. (4) to solve the IP, the amplitude and phase vectors associated with $q(s)$ are obtained. At this point, a rescaling operation $r^2 \to r$ to transform the above vectors from square to linear coordinates is done. In Figs. 1(a)–1(d) the corresponding two-dimensional masks due to the azimuthal rotation of them are shown. In particular, for the masks shown in Figs. 1(a) and 1(b) the profiles of the amplitude vectors are included as insets. For clarity's sake, in Figs. 1(c) and 1(d) only the central zone of the phase masks is plotted. In the last step, the spatial multiplexing technique of the DPM is employed to encode the amplitude and phase masks given in Figs. 1(b) and 1(d) into a single-phase DOE called FFDL, see Fig. 1(e). The spatial phase distribution of the FFDL is provided by Eq. (9). Hence, its optical surface is not circularly symmetric but shows phase jumps from one pixel to another, as one can see in the zoomed part of Fig. 1(e). These phase jumps correspond to a lens profile through the central line of the zoomed area. The origin of the phase jumps comes from the terms $\pm\cos^{-1}[\Lambda(x, y)/\Lambda_{\max}]$ given in Eqs. (6) and (7), which are responsible for the codification of the desired amplitude. Additionally, the high-frequency sampling in Eq. (8) causes phase jumps to happen among neighborhood pixels of the FFDL. So, the successful realization of FFDLs with commercial pho-SLMs may be conditioned by unwanted pixel crosstalk effects. That is why a correct mitigation of these effects [43,45] could be essential to bring the phase modulation in the pho-SLM closer to that expected from the theory. In the next section, crosstalk phenomenon is properly reduced while carrying out the practical demonstration of FFDLs.

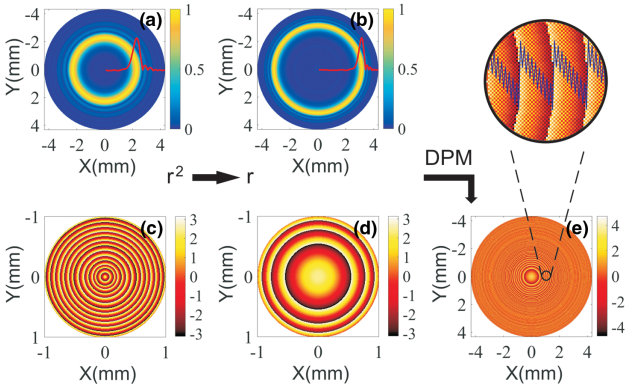

Fig. 1. Design of the freeform diffractive lens (FFDL). (a),(c) From the solution of the IP one can get the amplitude and phase masks in the square radial coordinate. (b),(d) After rescaling, corresponding masks in the radial coordinate are obtained. (e). Then, using the spatial multiplexing technique of the DPM, complex information is encoded into the final FFDL.

3. EXPERIMENT

In this section, the focusing properties of FFDLs are experimentally validated. To do that, two experiments are carried out. In the first one, the ability of programmable FFDLs to generate irradiance profiles with arbitrary shapes and different axial phase distributions is tested in amplitude. In the second experiment, the phase information imposed along the depth of focus is measured by using an indirect method proposed for this end. In Fig. 2, a photograph of the actual optical arrangement is shown. In addition, at the top-right part of this photograph, a schematic of the corresponding optical setup is included.

The laser beam emitted by a femtosecond laser oscillator is previously expanded with a commercial 6x reflective beam expander (Thorlabs—BE06R) to fix the transversal dimensions (15.36 mm × 8.64 mm) of the liquid crystal display. For simplicity, the above beam expansion procedure is not illustrated in Fig. 2. Then, the spectral content of the ultrashort pulse is reduced to a line of 10 nm full-width-at-half-maximum, centered at 800 nm, with the help of a bandpass filter **F** (Thorlabs—FBH800-10). In this way, the broadband radiation is transformed into a quasi-monochromatic laser beam with central wavelength at 800 nm. The **SLM** (Pluto-NIR-II, spatial resolution 1920 × 1080 pixels, 8 μm pixel pitch) was also optimized and calibrated for 800 nm. After filtering, the laser beam is sent to the **SLM** by using a 50:50 beam splitter **BS** (Venteon-BS0058). Consequently, half of the incident beam impinges perpendicular to the **SLM**, whereas the remaining light is blocked with a beam dump **BD** (Thorlabs—BT610). In the liquid crystal display, the beam is diffracted by the FFDL and focused back through the beam splitter to a CCD camera **CAM** (UI-3370CP-NIR-GL). To record images along the depth of focus, the camera was axially moved with stepped motors **SM** (Newport—MFA-CC UE1724SR). The total displacement of the motors is 66 mm. For the first experiment, all-tested FFDLs have focal lengths and axial focal depths fixed to $f = 200$ mm and $\Delta z = 50$ mm, respectively. Additionally, pixel crosstalk phenomenon happened in the pho-SLM were attenuated by using binary gratings $M_1(x, y)$ and $M_2(x, y)$ with more than 2 × 2 pixels per cell. The optimization process was carried out by progressively increasing the pixels per cell until the best approximation to the expected results was achieved [43,45]. For the used pho-SLM,

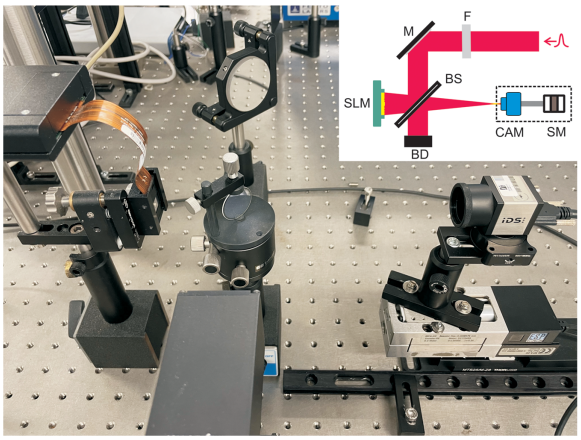

Fig. 2. Photograph of the actual optical arrangement, including optical setup (top-right part) used to measure the focusing properties of introduced FFDLs. It is mainly made up of the following components: bandpass filter **F**, silver mirror **M**, beam splitter **BS**, phase-only spatial light modulator **SLM**, beam dump **BD**, CCD camera **CAM**, and stepped motors **SM**.

acceptable results appeared when binary gratings had 3×3 pixels per cell, up to a maximum of 5×5 pixels per cell. The optimized pixel-cell size significantly decreased crosstalk effects, while keeping the diffraction orders of the gratings far enough apart to avoid their overlap at the focal region of the FFDL.

The results of the first experiment are shown in Fig. 3. Following the procedure described in Fig. 1, a set of four FFDLs was programmed to generate different intensity profiles, but the same linear phase ($\Theta(u) = \pi u$) along the axial focus was computer generated, see top-part of Fig. 3. To define phase functions $\Theta(u)$ within the phase range of the pho-SLM, the variable u was sampled within the interval $u \in [-1, 1]$ with N points. These intensity curves with arbitrary shapes bear out the power of FFDLs for tailoring the focal intensity of laser beams. Furthermore, as evidenced from the results achieved in Fig. 3, CBS also implies a predefined change of the axial phase along the focal region, which does not alter the shape of the expected intensity profiles. For this experiment, a super-Gaussian function $A(u) = e^{-u^{\gamma}/\sigma}$ (with $\gamma = 7$, $\sigma = 10^{-3}$), an increasing linear function $A(u) = u$, a sinusoidal function $A(u) = |\sin(\pi u)|$, and a cosine function $A(u) = |\cos(3\pi u/2)|$ were chosen as desired amplitude profiles in Figs. 3(a)–3(d), respectively. Measured intensity values were compared with corresponding numerical simulations of the on-axis diffracted field associated with each FFDL. Note that the measured light intensities are represented by small circle dots, whereas the corresponding theoretical values are represented by means of a continuous line. After a visual inspection of these curves, one realizes that measured data are in close agreement with the theoretical predictions. Small discrepancies between experiment and theory can be estimated by the calculus of the RMSE, resulting in the numerical values 3.7%, 2.2%, 4.9%, and 4.4%, respectively.

On the other hand, in Figs. 3(e)–3(h) another set of four FFDLs, this time giving rise to an intensity profile with a triangular shape ($A(u) = 1 - |u|$), but different axial phases were also tested. For this experience, the focal depth Δz associated to the triangular foci was increased from 20–50 mm with increments of 10 mm, as shown in Figs. 3(e)–3(h). From the attained results, it is apparent that phase encoding does not influence the look of intensity profiles. This confirms, from an experimental point of view, that CBS can be properly executed with independent election of amplitude and phase architectures. In particular, a linear phase function $\Theta(u) = \pi u$, a quadratic phase function $\Theta(u) = \pi u^2$, a cubic phase function $\Theta(u) = \pi u^3$, and a quartic phase function $\Theta(u) = \pi u^4$ were chosen in Figs. 3(e)–3(h), respectively. Again, the measured intensities fulfil very well with the theoretical expectations, exhibiting values of RMSE as low as 3.2%, 4.1%, 3.8%, and 4.4%, respectively.

To accomplish a complete validation of the focusing properties of FFDLs, measurements of the phase along the axial focus will be done. Owing to the relative-low spatial resolution of Shack-Hartmann wavefront sensors these commercial devices are not suitable for this task. Furthermore, the demand for one-dimensional phase analysis and possible fluctuations of the laser beam make the experiment even more challenging. At this point, an indirect method for axial phase measurement is introduced. It is based on the recording of the diffraction pattern corresponding to the coherent interference of two close and parallel foci generated from a complex multifocal lens $\upsilon(x, y)$. This lens contains the code of two FFDLs synthetized from the focusing elements $q_1(x, y)$ and $q_2(x, y)$, following the procedure described in Fig. 1. After a transversal displacement $\delta = np$ of each FFDL from the propagation axis of the laser beam, where n is an integer and $p = 8$ μm is the pixel pitch of the liquid crystal display, the complex multifocal lens is obtained from the following sum $\upsilon(x, y) \equiv q_2(x - \delta, y) + q_2(x + \delta, y)$. Again, the spatial multiplexing technique of the DPM is used to encode $\upsilon(x, y)$ into the pho-SLM. To calculate $q_1(x, y)$ and $q_2(x, y)$ by using Eq. (4) the amplitude $A(u)$ was fixed and defined by a super-Gaussian function, whereas the axial phase $\Theta(u)$ is allowed to vary among different functions. In these conditions, the axial phase of focused beams is determined by minimizing the difference between registered and simulated diffraction patterns. Owing to the fact that each diffraction pattern depends on the phase difference between foci $\Delta\Theta = [\Theta_1(u) - \Theta_2(u)]/2$, phase distortions due to optical aberrations in the plane of the liquid crystal display can be avoided. For the same reason, the present method is unable to pick up which function $\Theta_1(u)$ or $\Theta_2(u)$ goes to a particular focus. From the experiment, it was found that the spatial shape of recorded patterns significantly varies with the selection of the phase functions $\Theta_1(u)$ and $\Theta_2(u)$.

In the bottom-part of Fig. 4, three irradiance patterns, recorded with the camera at the transversal plane $z = 230$ mm are shown. The focal length $f = 200$ mm remains the same as before, whereas the focal depth $\Delta z = 60$ mm. The distance between parallel focused beams 2δ was set to 224 μm ($n = 14$). It ensures the generation of two separate focused beams. To check that, the transversal width w of one focus was estimated with the help of the TEM_{00} Gaussian beam model ($w \equiv \lambda f/(\pi a) \cong 12$ μm). Note also that

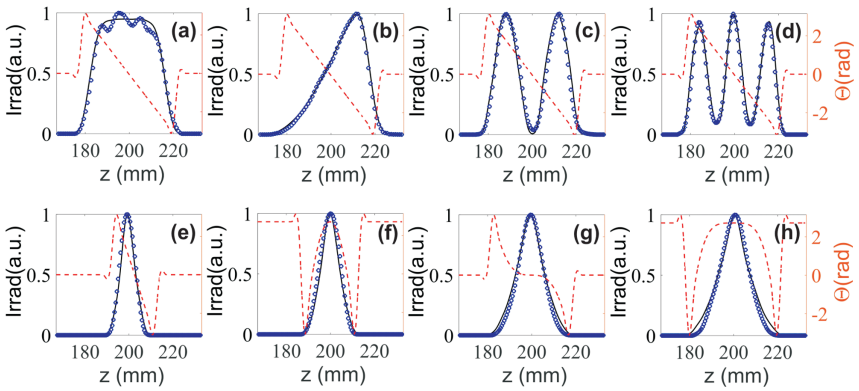

Fig. 3. Experimental and theoretical on-axis focal intensity and phase curves obtained by direct light diffraction on FFDLs. (top) Axial foci characterized by intensity curves with different shapes but the same linear phase. (bottom) Axial foci with intensity profiles of triangular shapes but different phase content.

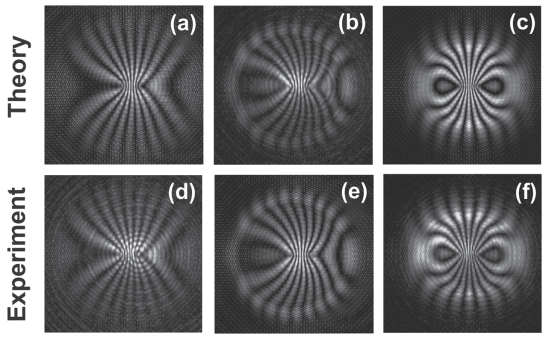

Fig. 4. (a)–(c) Theoretical and (d)–(f) experimental irradiance patterns originated by the coherent interference of two parallel foci. The electric fields associated with them have the same super-Gaussian amplitude but spatial phases given by (a),(d) linear and quadratic functions, (b),(e) sinusoidal and quadratic functions, and (c),(f) cosine and cosine functions.

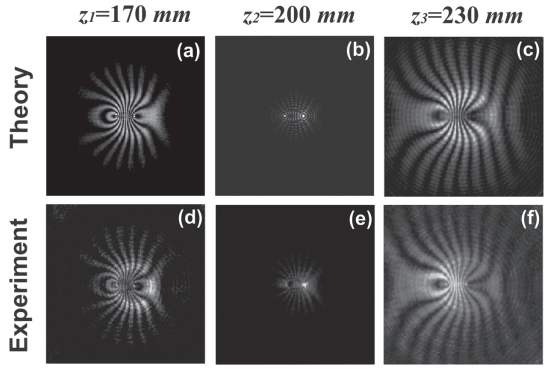

Fig. 5. (a)-(c) Theoretical and (d)-(f) experimental irradiance patterns originated by the coherent interference of two parallel foci at different transversal planes along the depth of focus. The electric fields associated with them have the same super-Gaussian amplitude but spatial phases given by minus sinusoidal and cubic functions.

the recording position ($z = 230$ mm) coincides with the position at which foci start to vanish, consequently they can hardly be seen from the irradiance patterns in Fig. 4.

In this experiment, the measured irradiance patterns are formed due to the codification of axial phase profiles defined by linear and quadratic functions $[\Theta_1(u) = \pi u,\ \Theta_2(u) = \pi u^2]$ in Fig. 4(d), sinusoidal and quadratic functions $[\Theta_1(u) = \pi\ \sin(\pi u),\ \Theta_2(u) = \pi u^2]$ in Fig. 4(e), or cosine and cosine functions $[\Theta_1(u) = \pi\ \cos(\pi u),\ \Theta_2(u) = \pi\ \cos(\pi u)$ in Fig. 4(f). Additionally, in Figs. 4(a)–4(c) the corresponding theoretical irradiance patterns assessed with the help of the Fresnel diffraction integral are included. For the numerical simulations, the influence of nondiffracted light coming from the pho-SLM on the recorded irradiance patterns was also considered. From Fig. 4, it is apparent that the spatial structure of diffraction patterns changes when modifying the phase content of focused light. This is the key point to support indirect phase measurements with the proposed method. The calculus of the RMSE between similar images corroborates that measured irradiance patterns retrieve the expected theoretical ones with high accuracy. For the cases shown in Figs. 4(a), 4(d), 4(b), 4(e), and 4(c), 4(f), numerical values of RMSE yield 8.3%, 9.5%, and 9.3%, respectively.

For further validation of the proposed method, the same experiment can be performed at different axial positions along the depth of focus. In this case, the shape of irradiance patterns should vary in less extension from one transversal plane to another. Measuring the interference light pattern in additional planes can be useful to rule out the ambiguity of having other combinations of prescribed amplitude and phase profiles that bring into a similar irradiance pattern. To show that, keeping the same experimental conditions as before, two foci with a super-Gaussian amplitude function and axial phase profiles defined by the functions $[\Theta_1(u) = -\pi\ \sin(\pi u),\ \Theta_2(u) = \pi u^3]$ were codified in a multifocal FFDL. The irradiance patterns measured at planes $z_1 = f - \Delta z/2$, $z_2 = f$, and $z_3 = f + \Delta z/2$ where $\Delta z = 60$ mm are shown in Figs. 5(d)–5(f), respectively. Again, corresponding theoretical irradiance patterns are shown in the top part of Figs. 5(a)–5(c). From Fig. 5, it is apparent that theory and experiment are in very good agreement, which is supported by RMSE values of 8.6%, 9,4%, and 9.7%, respectively. The results shown in Fig. 5 confirm the ability of FFDLs to modify the axial phase of focused coherent laser beams along the depth of focus.

4. FINAL REMARKS

The optical design of the FFDL allows compensating for wavefront deviations of the laser beam from the ideal plane wave. To do that, the wavefront $\alpha_{\text{real}}(x, y)$ associated with the input laser beam at the plane of the pho-SLM must be measured. After adding the complementary phase term into the lens function such as $e^{i[\alpha(x,y)-\alpha_{\text{real}}(x,y)]}$, the measured wavefront can be approached to a spatially uniform one. This precompensation procedure can help to obtain desired beam characteristics even when dealing with a convergent or divergent laser beam and/or under the presence of optical aberrations at the liquid crystal display.

As it might be inferred from the last experiment, the proposed beam shaping method can generate parallel foci, each one having a prescribed configuration of intensity and phase. For this purpose, a single multifocal lens $\upsilon(x, y)$, computer generated from the sum of $P \times Q$ off-axis focusing elements $q_{nm}(x, y)$, such that $\upsilon(x, y) \equiv \sum_{n=1}^{P} \sum_{m=1}^{Q} q_{nm}(x \pm \delta_{xn}, y \pm \delta_{ym})$, where δ_{xn} and δ_{ym} are transversal displacements in x and y directions, could be synthetized. Then, before sending $\upsilon(x, y)$ to the pho-SLM, it must be encoded into a single-phase mask by using the spatial multiplexing technique of the DPM. In principle, the maximum number of foci achieved with this method will basically depend on the technical specifications of the SLM. On one hand, the diameter of the encoded FFDLs should allow displacements δ_{xn} and δ_{ym} in the transversal directions of the pho-SLM's display without cutting their phase information. On the other hand, these displacements should avoid overlapping among the Bessel-like structure associated to each focus. For instance, for FFDLs designed with 1080 pixels in diameter and focal length $f = 200$ mm, the maximum number of foci achieved with a pho-SLM of spatial resolution 1920×1080 pixels can be roughly estimated on 12. In this case, the associated multifocal FFDL will cover the entire screen of the pho-SLM, and generated foci will be located equidistantly along a horizontal line.

In comparison with a Fresnel lens, the additional benefit of a FFDL related to the phase modulation comes at the expense of some energy losses at the focus. Note that, as the complex focusing element $q(x, y)$ is encoded by using a two-dimensional phase grating with transmission function $e^{i[M_1(x,y)\theta(x,y)+M_2(x,y)\vartheta(x,y)]}$, the available energy is redistributed among its different diffraction orders. Therefore, the amount of light sent to the focus of the FFDL (zero order of the grating) is not fixed, but it is conditioned

by the selection of the design parameters of the FFDL, i.e., the axial amplitude $A(u)$ and phase $\Theta(u)$ of the electric field, the focal depth Δz, or the focal length f. Numerical estimations of the diffraction efficiency of the FFDL for different sets of parameters indicate that intensity values greater than 25% of the light focused by the corresponding Fresnel lens are attainable. Furthermore, the diffraction efficiency of the FFDL can be finely modified by programming slightly changes in the phase function $\Theta(u)$, i.e., tuning its spatial shape or phase range continuously. For beam shaping applications that demand a precise control over the focal energy this programmable manipulation of the axial phase might be particularly interesting, i.e., in light-sheet microscopy due to the possibility to excite regions of interests with different energy thresholds, or in laser micro-processing to adjust the depth of ablation, without touching any components of the optical setup.

In the scalar theory of light, the intensity of coherent laser beams at the focal region can be tailored by using several types of refractive and/or diffractive focusing optical elements. However, without the ability to change, in a prescribed manner, the spatial phase of light, conventional beam shaping techniques can only provide a partial control over the focused light.

With the introduction of FFDLs it is possible to get complete and dynamic management of the amplitude and phase of coherent laser beams along the depth of focus. This kind of complex axial beam shaping, carried out with a single surface-pixeled diffractive lens, has additional benefits that include small thickness, low weight, or high efficiency. Nevertheless, when implementing with pho-SLMs the FFDLs maybe limited by the spatial resolution these liquid crystal devices, their phase response to abrupt phase jumps (crosstalk effects), the operating wavelength range, or the laser-induced damage threshold. In contrast, the direct fabrication of FFDLs by advanced lithography techniques, i.e., photolithography or electron beam lithography could reduce the above limitations due to the high accuracy in manufacturing demonstrated by these fabrication techniques. Hence, this direct fabrication may allow decreasing the pixel pitch, reducing crosstalk effects, and working with high power laser radiations whose energies can reach values above the damage threshold of commercially available pho-SLMs.

I believe that the extra degree of freedom provided by a prescribed phase modulation along the depth of focus should impact several photonic applications related to the interaction of coherent laser beams with matter such as laser materials processing, linear and nonlinear microscopy, digital holography, generation of nonlinear optical effects under ultrashort pulsed illumination, light propagation through turbid media, generation of optical vortices, or optical encryption.

Funding. Ministerio de Ciencia e Innovación (MCIN/AEI/10.13039/501100011033); Universitat Jaume I (UJI-B2022-38); Generalitat Valenciana (PROMETEO/2020/029).

Acknowledgment. The author thanks Dr. Gladys Mínguez-Vega for her fruitful comments and discussions on this work. The author is very grateful to the "Serveis Centrals d'Instrumentación Científica" (SCIC) of the University Jaume I for the use of the laser facilities. This publication is part of Project No. PID2021-124814NB-C22, funded by MCIN/AEI/10.13039/501100011033, "FEDER, A way of making Europe."

Disclosures. The author declares no conflicts of interest.

Data availability. No data were generated or analyzed in the presented research.

REFERENCES

1. P. Torres-Sánchez, I. Porras, N. Ramos-Chernenko, F. A. de Saavedra, and J. Praena, "Optimized beam shaping assembly for a 2.1-MeV proton-accelerator-based neutron source for boron neutron capture therapy," Sci. Rep. **11**, 7576 (2021).
2. A. Zannotti, C. Denz, M. A. Alonso, and M. R. Dennis, "Shaping caustics into propagation-invariant light," Nat. Commun. **11**, 3597 (2020).
3. D. Wei, C. Wang, X. Xu, H. Wang, Y. Hu, P. Chen, J. Li, Y. Zhu, C. Xin, X. Hu, Y. Zhang, D. Wu, J. Chu, S. Zhu, and M. Xiao, "Efficient nonlinear beam shaping in three-dimensional lithium niobate nonlinear photonic crystals," Nat. Commun. **10**, 4193 (2019).
4. K. Petelczyc, A. Kolodziejczyk, N. Błocki, A. Byszewska, Z. Jaroszewicz, K. Kakarenko, K. Kołacz, M. Miler, A. Mira-Agudelo, W. Torres-Sepúlveda, and M. Rękas, "Model of the light sword intraocular lens: in-vitro comparative studies," Biomed. Opt. Express **11**, 40–54 (2020).
5. C. H. Yang and A. Y. G. Fuh, "Complex beam shaping based on an equivalent Q-plate system and analysis of its properties using digital holography polarization imaging," Sci. Rep. **7**, 2769 (2017).
6. S. P. Murzin, "Improvement of thermochemical processes of laser-matter interaction and optical systems for wavefront shaping," Appl. Sci. **12**, 12133 (2022).
7. X. Ding, Y. Ren, and R. Lu, "Shaping super-Gaussian beam through digital micro-mirror device," Sci. China Phys. Mech. Astron. **58**, 1–6 (2015).
8. T. Gissibl, M. Schmid, and H. Giessen, "Spatial beam intensity shaping using phase masks on single-mode optical fibers fabricated by femtosecond direct laser writing," Optica **3**, 448–451 (2016).
9. J. Li, Z. Kuang, S. Edwardson, W. Perrie, D. Liu, and G. Dearden, "Imaging-based amplitude laser beam shaping for material processing by 2D reflectivity tuning of a spatial light modulator," Appl. Opt. **55**, 1095–1100 (2016).
10. J. Yang, D. Lin, D. Bao, and S. Tao, "Pixel level control of amplitude, phase, and polarization of an arbitrary vector beam," Appl. Phys. Lett. **121**, 191103 (2022).
11. L. Wu, S. Cheng, and S. Tao, "Simultaneous shaping of amplitude and phase of light in the entire output plane with a phase-only hologram," Sci. Rep. **5**, 15426 (2015).
12. M. Woerdemann, C. Alpmann, M. Esseling, and C. Denz, "Advanced optical trapping by complex beam shaping," Laser Photon. Rev. **7**, 839–854 (2013).
13. S. Mohammadou, B. Mohamadou, and G. Montemezzani, "Complex beam shaping by cascaded conical diffraction with intercalated polarization transforming elements," Opt. Express **25**, 25392–25406 (2017).
14. W. Ji, C. H. Lee, P. Chen, W. Hu, Y. Ming, L. Zhang, T.-H. Lin, V. Chigrinov, and Y.-Q. Lu, "Meta-Q-plate for complex beam shaping," Sci. Rep. **6**, 25528 (2016).
15. K. Falaggis, J. Rolland, F. Duerr, and A. Sohn, "Freeform optics: introduction," Opt. Express **30**, 6450–6455 (2022).
16. S. Schmidt, S. Thiele, A. Toulouse, C. Bösel, T. Tiess, A. Herkommer, H. Gross, and H. Giessen, "Tailored micro-optical freeform holograms for integrated complex beam shaping," Optica **7**, 1279–1286 (2020).
17. Z. Feng, B. D. Froese, R. Liang, D. Cheng, and Y. Wang, "Simplified freeform optics design for complicated laser beam shaping," Appl. Opt. **56**, 9308–9314 (2017).
18. S. Wei, Z. Zhu, Z. Fan, Y. Yan, and D. Ma, "Double freeform surfaces design for beam shaping with non-planar wavefront using an integrable ray mapping method," Opt. Express **27**, 26757–26771 (2019).
19. C. Bösel and H. Gross, "Double freeform illumination design for prescribed wavefronts and irradiances," J. Opt. Soc. Am. A **35**, 236–243 (2018).
20. Z. Feng, L. Huang, G. Jin, and M. Gong, "Designing double freeform optical surfaces for controlling both irradiance and wavefront," Opt. Express **21**, 28693–28701 (2013).
21. S. Chang, R. Wu, L. An, and Z. Zheng, "Design beam shapers with double freeform surfaces to form a desired wavefront with prescribed illumination pattern by solving a monge-ampère type equation," J. Opt. **18**, 125602 (2016).
22. V. Oliker, L. L. Doskolovich, and D. A. Bykov, "Beam shaping with a plano-freeform lens pair," Opt. Express **26**, 19406–19419 (2018).
23. C. Bösel, N. G. Worku, and H. Gross, "Ray-mapping approach in double freeform surface design for collimated beam shaping beyond the paraxial approximation," Appl. Opt. **56**, 3679–3688 (2017).

24. R. M. Wood, *Laser-Induced Damage of Optical Materials*, 1st ed. (CRC Press, 2003).
25. J.-Y. Natoli, L. Gallais, H. Akhouayri, and C. Amra, "Laser-induced damage of materials in bulk, thin-film, and liquid forms," Appl. Opt. **41**, 3156–3166 (2002).
26. G. C. Bhar, A. K. Chaudhary, and P. Kumbhakar, "Study of laser induced damage threshold and effect of inclusions in some nonlinear crystals," Appl. Surf. Sci. **161**, 155–162 (2000).
27. B. C. Stuart, M. D. Feit, S. Herman, A. M. Rubenchik, B. W. Shore, and M. D. Perry, "Nanosecond-to-femtosecond laser-induced breakdown in dielectrics," Phys. Rev. B **53**, 1749 (1996).
28. J. S. Liu, A. J. Caley, and M. R. Taghizadeh, "Diffractive optical elements for beam shaping of monochromatic spatially incoherent light," Appl. Opt. **45**, 8440–8447 (2006).
29. L. De Sio, D. E. Roberts, Z. Liao, J. Hwang, N. Tabiryan, D. M. Steeves, and B. R. Kimball, "Beam shaping diffractive wave plates [invited]," Appl. Opt. **57**, A118–A121 (2018).
30. R. Dharmavarapu, S. Bhattacharya, and S. Juodkazis, "Diffractive optics for axial intensity shaping of Bessel beams," J. Opt. **20**, 085606 (2018).
31. J. Shao, T. Haase, R. Zhang, C. Aguergaray, N. Broderick, and S. Sun, "Focusing flattop beam shaping with complex modulation holography," AIP Adv. **11**, 105118 (2021).
32. J. Liang, R. N. Kohn, Jr., M. F. Becker, and D. J. Heinzen, "High-precision laser beam shaping using a binary-amplitude spatial light modulator," Appl. Opt. **49**, 1323–1330 (2010).
33. H. Ma, P. Zhou, X. Wang, Y. Ma, F. Xi, X. Xu, and Z. Liu, "Near-diffraction-limited annular flattop beam shaping with dual phase only liquid crystal spatial light modulators," Opt. Express **18**, 8251–8260 (2010).
34. C. W. McCutchen, "Generalized aperture and the three-dimensional diffraction image," J. Opt. Soc. Am. **54**, 240–244 (1964).
35. J. A. Davis, C. S. Tuvey, O. López-Coronado, J. Campos, M. J. Yzuel, and C. Iemmi, "Tailoring the depth of focus for optical imaging systems using a Fourier transform approach," Opt. Lett. **32**, 844–846 (2007).
36. P. N. Gundu, E. Hack, and P. Rastogi, "High efficient superresolution combination filter with twin LCD spatial light modulators," Opt. Express **13**, 2835–2842 (2005).
37. J. A. Davis, D. M. Cottrell, J. Campos, M. J. Yzuel, and I. Moreno, "Encoding amplitude information onto phase-only filters," Appl. Opt. **38**, 5004–5013 (1999).
38. A. Márquez, C. Iemmi, J. C. Escalera, J. Campos, S. Ledesma, J. A. Davis, and M. J. Yzuel, "Amplitude apodizers encoded onto Fresnel lenses implemented on a phase-only spatial light modulator," Appl. Opt. **40**, 2316–2322 (2001).
39. V. Arrizón and D. Sánchez-de-la-Llave, "Double-phase holograms implemented with phase-only spatial light modulators: performance evaluation and improvement," Appl. Opt. **41**, 3436–3447 (2002).
40. H. Song, G. Sung, S. Choi, K. Won, H. S. Lee, and H. Kim, "Optimal synthesis of double-phase computer generated holograms using a phase-only spatial light modulator with grating filter," Opt. Express **20**, 29844–29853 (2012).
41. X. Sui, Z. He, H. Zhang, L. Cao, D. Chu, and G. Jin, "Spatiotemporal double-phase hologram for complex-amplitude holographic displays," Chin. Opt. Lett. **18**, 100901 (2020).
42. O. Mendoza-Yero, G. Mínguez-Vega, and J. Lancis, "Encoding complex fields by using a phase-only optical element," Opt. Lett. **39**, 1740–1743 (2014).
43. J. A. Davis, E. D. Wolfe, I. Moreno, and D. M. Cottrell, "Encoding complex amplitude information onto phase-only diffractive optical elements using binary phase Nyquist gratings," OSA Contin. **4**, 896–910 (2021).
44. O. Mendoza-Yero, "Complex shaping of the depth of focus," OSA Contin. **3**, 2175–2184 (2020).
45. M. Carbonell-Leal and O. Mendoza-Yero, "Effects of mitigation of pixel cross-talk in the encoding of complex fields using the double-phase method," Opt. Eng. **59**, 041203 (2019).